

Accepted Manuscript

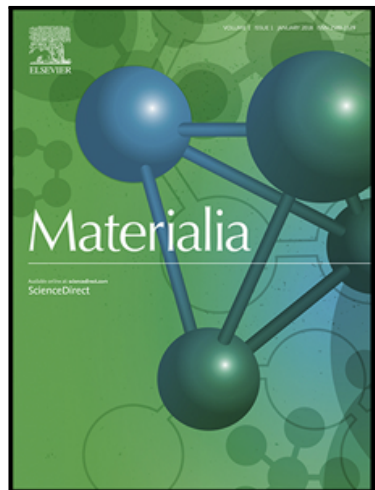
Indentation size effects in spherical nanoindentation analyzed by experiment and non-local crystal plasticity

J.K. Engels, S. Gao, W. Amin, A. Biswas, A. Kostka, N. Vajragupta,
A. Hartmaier

PII: S2589-1529(18)30161-3

DOI: <https://doi.org/10.1016/j.mtla.2018.09.032>

Reference: MTLA 125



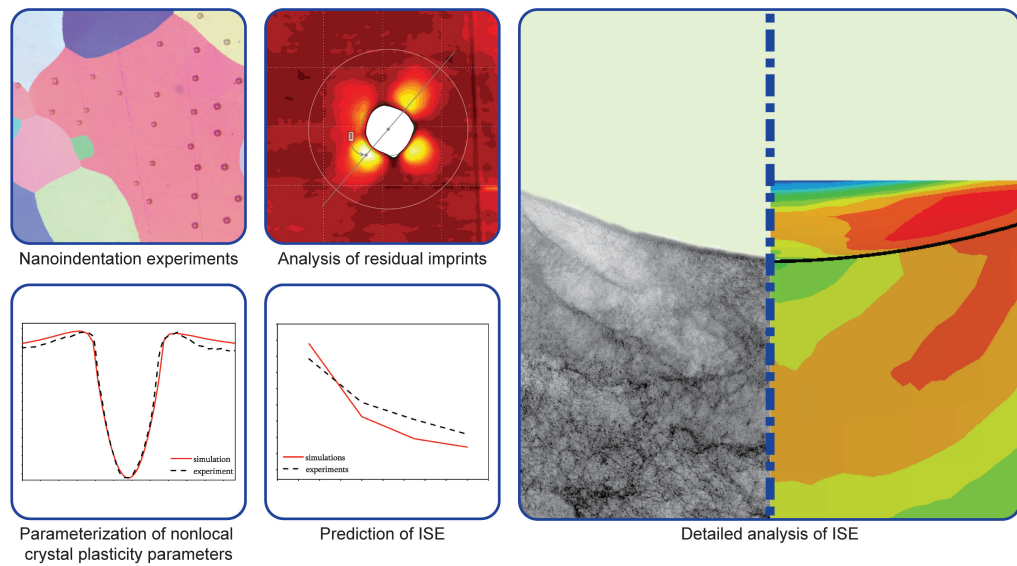
To appear in: *Materialia*

Received date: 21 September 2018

Accepted date: 24 September 2018

Please cite this article as: J.K. Engels, S. Gao, W. Amin, A. Biswas, A. Kostka, N. Vajragupta, A. Hartmaier, Indentation size effects in spherical nanoindentation analyzed by experiment and non-local crystal plasticity, *Materialia* (2018), doi: <https://doi.org/10.1016/j.mtla.2018.09.032>

This is a PDF file of an unedited manuscript that has been accepted for publication. As a service to our customers we are providing this early version of the manuscript. The manuscript will undergo copyediting, typesetting, and review of the resulting proof before it is published in its final form. Please note that during the production process errors may be discovered which could affect the content, and all legal disclaimers that apply to the journal pertain.



Indentation size effects in spherical nanoindentation analyzed by experiment and non-local crystal plasticity

J. K. Engels^{a,*}, S. Gao^a, W. Amin^a, A. Biswas^a, A. Kostka^b, N. Vajragupta^a,
A. Hartmaier^a

^a*Interdisciplinary Centre for Advanced Materials Simulation, Ruhr-Universität Bochum,
Universitätsstr. 150, 44801 Bochum, Germany*

^b*Zentrum für Grenzflächendominierte Hochleistungswerkstoffe, Ruhr-Universität Bochum,
Universitätsstr. 150, 44801 Bochum, Germany*

Abstract

Nanoindentation has become a rather mature tool to characterize and measure mechanical properties of materials on micro- and nanometer length scales. However, the different types of indentation size effects (ISE) hamper the assessment of true, i.e., scale independent, material properties by nanoindentation. In the present study, the mechanisms of the ISE in spherical indentation have been investigated and quantified. Furthermore, it has been shown that the determination of non-local crystal plasticity parameters from nanoindentation results is possible. The thus-parameterized non-local crystal plasticity describes the higher-order size effect occurring in spherical indentation correctly and offers the possibility to understand the mutual contributions of geometrically necessary dislocations (GND) and statistically stored dislocations (SSD) to the material response. Nanoindentation experiments have been performed into a single grain of an ARMCO iron specimen, where the load displacement curves have been recorded, and the post-indentation surface topologies have been characterized. Furthermore, transmission electron microscopy has been performed to analyse the plastically deformed volume beneath the indentation. By comparing experimental and numerical nanoindentation results with respect to the plastic zone and dislocation structures, we validate the non-local crystal plas-

*Corresponding author. Tel. +49 234 32 22247.
Email address: jenni.zglinski@rub.de (J. K. Engels)

ticity model of indentation and increase our understanding of the underlying mechanisms of the ISE in spherical indentation.

Keywords: Crystal Plasticity, Nanoindentation, Indentation Size Effect

1. Introduction

Nanoindentation has evolved into a standard tool to investigate plasticity on small length scales. The most obvious results, the load-displacement curves, deliver mechanical properties such as indentation hardness, anisotropic elastic properties, and yield behavior. However, load-displacement data alone do not provide further material information such as the topology of the surrounding area of residual imprints. Exemplarily, the pile-up formation needs to be considered to determine the projected contact area between the indenter tip and material by using the tip area function method [1]. It was found that the evolution of a pile-up depends on the maximum indentation force, work-hardening conditions, and crystallographic orientation of the indented material [2]. A third interesting aspect of the nanoindentation technique is the phenomenon of indentation size effect (ISE), which is defined as an increase in apparent hardness with a) decreasing indenter size or b) smaller indentation depth. This effect was observed in several experimental studies, see e.g., [3, 4, 5] and traced back to the formation of so-called geometrically necessary dislocations (GNDs), for which theoretical concepts originate in the 1950s [6, 7, 8]. In this regard, [9] performed indentation in a fcc metal using a wedge indenter tip on a single crystal. With the help of Orientation Imaging Microscopy (OIM) all non-zero components of the Nye dislocation density tensor were calculated and an analytical expression for the lower bound of the total GND density was derived. Furthermore, similar technique was used by [10] to measure GND densities associated with different angles of wedge indenter tips. For nanoindentation, various phenomenological models were designed: Fleck and Hutchinson [11, 12] developed a model for describing the ISE, which introduced a material length scale into a phenomenological model. Ashby [8] introduced GNDs for indentation with a flat punch.

Nix and Gao [13] extended the model for conical indenters and Swadener for spherical indenter tips [3]. These studies showed that the hardness depends on indenter radius and the maximum displacement of the indentation. Since similar size effects are also responsible for the grain-size dependence of the strength in polycrystals (grain boundaries with large misorientation produce considerable strain gradients and hence GNDs), it is instructive to study ISE to gain insight into the role of GNDs during plastic deformation.

In order to resolve the heterogeneous evolution of plastic flow, lattice rotation and dislocations under the indenter, Crystal Plasticity Finite Element Modeling (CPFEM) can be employed because it combines the fundamental physical concepts of elastoplasticity of metals with established numerical methods, see e.g., [14]. Since its emergence, CPFEM has grown to a great level of maturity, and a broad spectrum of numerical schemes and constitutive formulations are able to mimic various aspects of mechanical behavior of single- and polycrystals [15, 16, 17, 18]. Furthermore, crystal plasticity simulations can be directly compared with experimental findings for in-depth study of various quantities including, but not limited to, strain, strain rates, strain paths, shear rates, local stresses, forces, texture evolution and various size effects, [19, 4]. However, CPFEM models in their standard form neglect the influence of strain gradients and cannot describe size effects, which are important aspects of nanoindentation. For allowing CPFEM to treat non-local deformation mechanisms and to capture the indentation size effect, gradients in the plastic strains have to be determined and translated to GND density state variables [20, 21, 22]. In this study, we propose a model that considers the influence of complex microstructural features on the mechanical response of the material. Therefore, a large number of parameters is necessary to describe the specific and unique material behavior.

CPFEM simulations of nanoindentation have been performed by several authors, both with local [23, 24] or, more recently, with non-local formulations [25, 23, 26]. The objective of the present work is to predict the indentation size effect by combining both experimental and numerical work. In order to accom-

plish this, it is important to parameterize the non-local CP model by Ma et al. [27] for pure or ARMCO iron¹ in a first step. With its comparably large grain sizes ARMCO iron is well suited to identify previously selected grain orientation. The present study is structured as follows: First, the nanoindentation experimental setup and analysis script are described. The following parameterization of our non-local crystal plasticity model is achieved by inverse analysis. Based on a direct comparison between the parameterized nanoindentation model and the experimental results, the indentation size effect is analyzed and interpreted.

2. Experimental Methods

2.1. Nanoindentation and AFM

During nanoindentation tests, load-displacement curves were recorded as shown in Figure 5(a). Nanoindentation experiments were performed with a spherico-conical tip of 5 μm radius in a previously selected single crystal with a grain orientation close to $<001>$, which is represented in Figure 1(a). The indentation tip had been calibrated by fused silica indentation. Following maximum indentation forces have been applied in this project: 12.5 mN, 15 mN, 17.5 mN and 20 mN, and all load-controlled experiments were performed with a loading rate of 1 mN/s. Unloading started immediately after a holding period of 10 seconds. For the same material, tensile tests had been perfomed by Schmaling in a previous study, [28], and a representative flow curve providing more information about the material behavior, especially in the context of parameterization of crystal plasticity values, is shown in Figure 1(b). Note that the work-hardening rate is rather small.

After completing all nanoindentation tests, residual imprints were characterized using the Atomic Force Microscope (AFM) to measure a high-resolution surface topography up to the nanometer scale.

¹ARMCO iron, a trade name for technically pure iron with a purity of 99.8 - 99.9% is selected as the testing material.

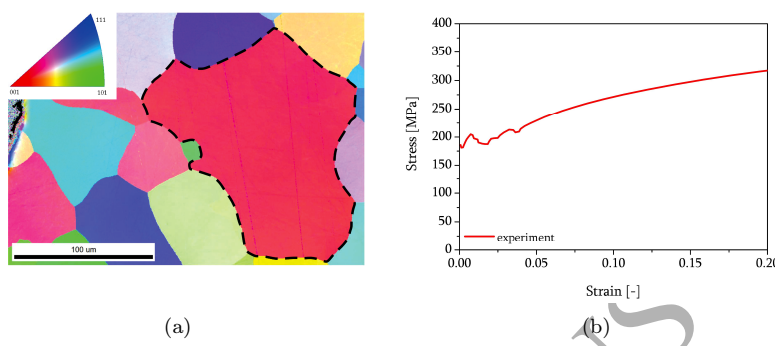


Figure 1: General overview of ARMCO iron. (a) EBSD figure of nanoindented area with grain orientation close to $<100>$. (b) experimentally observed flow curve of used alloy, courtesy of [28].

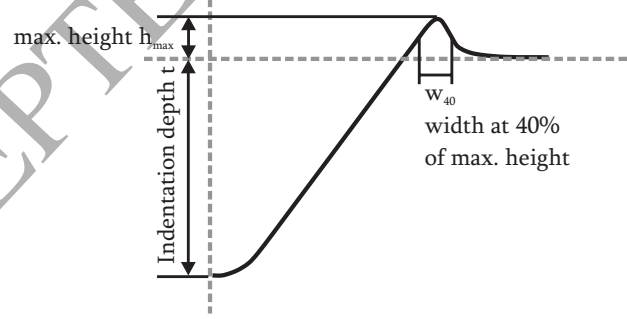


Figure 2: Schematic diagram of the residual imprint with quantitative parameters.

Table 1: Summary of characteristic dimensions of the residual imprints for different indentation forces. Obtained both from experiment and numerical simulation.

Indentation force (mN)	t (nm)		h_{\max} (nm)		$w_{40\%}$ (nm)	
	num	exp	num	exp	num	exp
12.5	-298	-295	39	27	1965	2152
15.0	-361	-360	43	48	2488	2201
17.5	-412	-419	48	54	3216	2622
20.0	-469	-477	56	75	3453	2648

2.2. Quantitative Analysis of Residual Imprints

For the purpose of comparing experiments and simulations, the residual imprints were quantitatively analyzed using an in-house script which can handle both numerical and experimental results. The basic ideas of the evaluation method come from the publications of [28], [29] and have been refined for the present work. First, indentation depth t , maximum height h_{\max} , and pile-up width at 40% of maximum height $w_{40\%}$, see Figure 2, were evaluated. These quantitative analysis results (along with numerical results which will be discussed later) were summarized in Table 1. For the second step, a two dimensional topology line for each residual imprint was created from a line passing through minimum as well as local maximum (at pile-ups). Because the surface plane of an indented grain was close to $\langle 001 \rangle$, four-fold pile-up symmetry was expected. As a representative example of the clear and comprehensible method, Figure 3 illustrates several residual imprints in the same grain with a maximum indentation load of 17.5 mN. The comparison shows consistent results and thus the quality of the present approach.

3. Nanoindentation Simulation and Material Parameters Identification

A finite element model was used to investigate the deformation mechanisms below the indenter in combination with the observed size effect. In this section, this non-local crystal plasticity model, as well as the parameterization of material parameters are described.

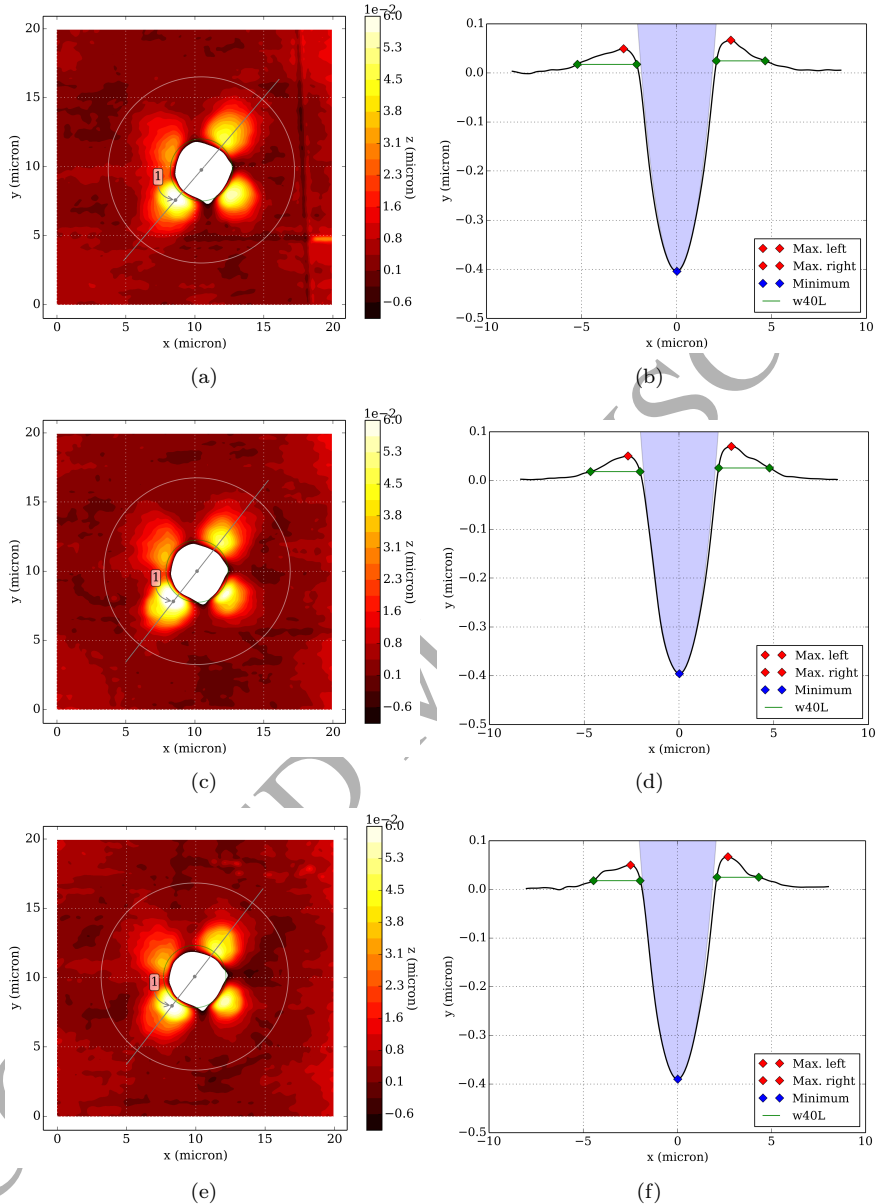


Figure 3: Top view of surface topology for (left column) three individual indentations in same grain with maximum indentation force of 17.5 mN. Corresponding topography lines along line through maximum pileup and centre are shown in figure (right column).

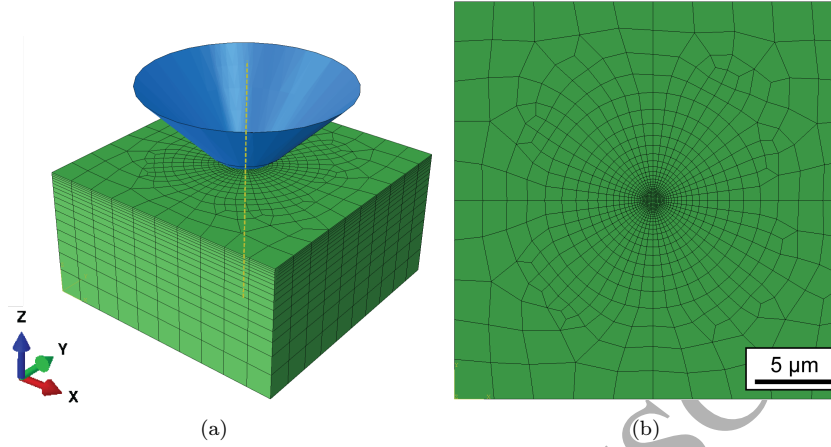


Figure 4: Finite-element model of nanoindentation: (a) the overall view; (b) mesh configuration at the contact surface of the single grain model.

3.1. Nanoindentation Simulations

The nanoindentation model used in this study is shown in Figure 4. This numerical model excludes the symmetry and considers the whole experimental set-up. The dimension of the indented single grain was $25 \times 25 \times 13 \text{ } \mu\text{m}^3$, which was sufficiently large to cover the occurred plastic zone from the nanoindentation test. To accommodate a strong deformation field at the contact area and to accurately calculate strain gradients, the mesh was locally severely refined. The smallest element size at the contact region was $0.0823 \text{ } \mu\text{m}$ (approx. 1.5% of the indenter radius) with radially increasing element size. This numerical model was meshed with 8-node linear brick (C3D8) and finally consisted of 18,544 elements. The spherico-conical indenter was modelled as an analytical rigid body, and the contact between indenter and grain was assumed to be frictionless. The loading scheme assigned to the numerical model was identical to the experimental one described in the previous section.

3.2. A non-local Crystal Plasticity Model

Within the scope of this work, a non-local crystal plasticity model proposed by Ma et al. [27] was applied. Since this crystal plasticity model follows fun-

damental concepts of established work [30, 31, 32], we limited ourselves to the details of the non-local formulation and the relevant material parameters. From the kinematics of deformation, the total deformation gradient \mathbf{F} can be multiplicatively decomposed into the elastic deformation gradient \mathbf{F}_e and the plastic deformation gradient \mathbf{F}_p ,

$$\mathbf{F} = \mathbf{F}_e \mathbf{F}_p. \quad (1)$$

The elastic deformation is calculated by Hooke's law. For the plastic deformation, the plastic velocity gradient \mathbf{L}_p , which is a function of the plastic deformation gradient \mathbf{F}_p , can be described as

$$\mathbf{L}_p = \dot{\mathbf{F}}_p \mathbf{F}_p^{-1}. \quad (2)$$

In this study, only crystallographic slip of dislocations is considered as mechanism for plastic deformation. Thus, \mathbf{L}_p is taken as the sum of the shear rates of all N slip systems

$$\mathbf{L}_p = \sum_{\alpha=1}^N \dot{\gamma}_\alpha \mathbf{M}_\alpha, \quad (3)$$

where $\dot{\gamma}_\alpha$ is the plastic shear rate, and $\mathbf{M}_\alpha = \mathbf{d}_\alpha \otimes \mathbf{n}_\alpha$ is the Schmid tensor for the slip system α , which is defined by the slip direction \mathbf{d}_α and the slip plane normal \mathbf{n}_α . The symbol \otimes denotes the dyadic product of two vectors resulting in a second rank tensor. The total number of slip systems is N .

According to the non-local model proposed by Ma et al. [27], the flow rule and the hardening law can be expressed, respectively, as

$$\dot{\gamma}_\alpha = \dot{\gamma}_0 \left| \frac{\tau_\alpha + \tau_\alpha^{\text{GNDk}}}{\hat{\tau}_\alpha + \hat{\tau}_\alpha^{\text{GNDi}}} \right|^{p_1} \text{sgn}(\tau_\alpha + \tau_\alpha^{\text{GNDk}}), \quad (4)$$

and

$$\dot{\hat{\tau}}_\alpha = \sum_{\beta=1}^N h_0 \chi_{\alpha\beta} \left(1 - \frac{\hat{\tau}_\alpha}{\hat{\tau}_{\text{sat}}} \right)^{p_2} |\dot{\gamma}_\beta|, \quad (5)$$

where $\dot{\gamma}_0$ is the reference shear rate, p_1 is the inverse value of the strain rate sensitivity, h_0 is the reference hardening parameter, and $\chi_{\alpha\beta}$ is the cross hardening matrix which is assigned as 1.0 for coplanar slip systems and 1.4 otherwise. $\hat{\tau}_{\text{sat}}$ is the saturation slip resistance, and p_2 is a fitting parameter. The initial value

of the slip resistance $\hat{\tau}_\alpha$ is defined as $\hat{\tau}_0$. $\text{sgn}()$ is a mathematical function that extracts the sign of a real number. The resolved shear stress τ_α for each slip system can be calculated from the stress $\tilde{\mathbf{S}}_\alpha$ in the intermediate configuration as

$$\tau_\alpha = \tilde{\mathbf{S}}_\alpha : \mathbf{M}_\alpha. \quad (6)$$

The flow rule in equation (4) consists of two additional back stresses $\tau_\alpha^{\text{GNDk}}$ and $\hat{\tau}_\alpha^{\text{GNDi}}$ describing the hardening caused by geometrically necessary dislocations (GNDs) [27]. The non-local constitutive model in this context is derived from the concept of super GNDs densities and incorporates the plastic strain gradient. The hardening due to plastic strain gradients is split up into an isotropic hardening part $\hat{\tau}_\alpha^{\text{GNDi}}$ and a kinematic hardening part $\tau_\alpha^{\text{GNDk}}$.

The second rank dislocation density tensor \mathbf{G} in the reference configuration is computed from the curl of \mathbf{F}_p as introduced by Nye [6]

$$G_{ij} = -(\mathbf{F}_p \times \nabla)_{ij}. \quad (7)$$

It must be noted that a reconstruction of meaningful crystallographic dislocation populations in a unique way is impossible because the dislocation density tensor only contains information about averages of dislocations and residual Burgers vectors. However, a unique definition of super GNDs is achievable by projecting the dislocation density tensor to the global Cartesian coordinates of the system. Consequently, the stress fields of the crystallographic GNDs can be described with good accuracy [27], and the GND density tensor can be separated into nine independent parts $\bar{\rho}_\alpha$ by evaluating

$$\sum_{\alpha=1}^9 \bar{\rho}_\alpha \bar{\mathbf{d}}_\alpha \otimes \bar{\mathbf{t}}_\alpha = \frac{1}{b} \mathbf{G}, \quad (8)$$

where $\bar{\mathbf{d}}_\alpha$ and $\bar{\mathbf{t}}_\alpha$ are permutations of the Cartesian unit vectors as determined in [27] and b is the magnitude of the crystallographic Burgers vector. The super GND densities for $\alpha = 1, 2, 3$ represent screw-type superdislocations, while the remaining components represent edge-type superdislocations, which are vital for determining the internal stress fields as a consequence of the super GNDs.

The isotropic hardening for dislocation slip contributed by these super GNDs is expressed in a Taylor-type equation

$$\hat{\tau}_\alpha^{\text{GNDi}} = c_1 \mu b \sqrt{\sum_{\beta=1}^9 \chi_{\alpha\beta}^{\text{GND}} |\bar{\rho}_\beta|}, \quad (9)$$

where c_1 is the Taylor hardening coefficient or a geometrical factor [38] and μ is the shear modulus. $\chi_{\alpha\beta}^{\text{GND}}$ is the cross hardening matrix between crystallographic mobile dislocations and super GNDs.

The long-range internal stresses caused by GNDs in dislocation pile-ups contribute to another hardening effect. This part is calculated by evaluating the second order gradient of \mathbf{F}_p , which results in a super GND gradient $\bar{\rho}_{\alpha,I}$ in the form of

$$\bar{\rho}_{\alpha,I} = \frac{1}{b} G_{jk,I} \bar{d}_{\alpha j} \bar{t}_{\alpha k}. \quad (10)$$

By evaluating these gradients within a small volume of dimension L^3 , the internal stresses $\tilde{\mathbf{S}}^{\text{GND}}$ in the intermediate configuration caused by dislocation pile-ups at grain boundaries can be calculated as explained in [27]. The parameter L is a model parameter related to the average dislocation spacing. Thus, the kinematic hardening can be given by

$$\tau_\alpha^{\text{GNDk}} = \tilde{\mathbf{S}}^{\text{GND}} \cdot \mathbf{M}_\alpha. \quad (11)$$

Within the scope of this study, the aforementioned constitutive laws were directly implemented. As the crystal structure of the investigated material is BCC, dislocation slip on the common crystallographic $\langle 111 \rangle \{110\}$ slip systems was considered.

3.3. Parameterization of non-local Crystal Plasticity Model

To determine the non-local crystal plasticity parameters, the nanoindentation model was coupled to the non-local crystal plasticity model via a user-defined material subroutine (UMAT) within Abaqus, [33], and the parameters were adapted to fit both load-displacement curves and residual surface topologies. It must be noted that the parameterization process was an iterative FE

approach and started from the crystal plasticity parameters of ARMCO iron as given in [28]. In difference to the local crystal plasticity formulation used in [28], the present study introduced two key non-local parameters, L and c_1 . L is related to the average dislocation spacing as mentioned above. From Fig. 6, the dislocation density beneath the indented area is high. This is the reason why for L a small value has been chosen, corresponding to a few Burgers vectors. c_1 is a fitting parameter to control the Taylor hardening effect due to GNDs. In the first step, non-local crystal plasticity parameters were varied to match nanoindentation simulation with experimentally observed load-displacement- and topology-data for the case of an applied maximum load of 15 mN. With respect to the residual imprint, quantitative analysis results and a two-dimensional topology line were used as references. By comparison of the load-displacement curves in Figure 5(a), the two-dimensional topology line shown in Figure 5(c), and the quantitative analysis results summarized in Table 1, we can conclude a good agreement between nanoindentation simulation and experiment obtained for the loading case of 15 mN. To achieve a unique solution of parameterization, nanoindentation simulations were conducted for other applied maximum loads using calibrated non-local crystal plasticity parameters. As illustrated in Figures 5(b), (d) and (e), nanoindentation simulations using this parameters set conform with the experiments, despite small deviations for the load-displacement curve at larger applied maximum load and the topology line at lower applied maximum load. Therefore, the obtained non-local crystal plasticity parameters of ARMCO iron are considered suitable for describing deformation behavior of this steel grade. Table 2 summarizes calibrated non-local crystal plasticity parameters of ARMCO iron.

In this study, the hardness of both nanoindentation simulations and experiments were calculated with the help of Oliver & Pharr method [1], which is also known as Multiple-Point Unload Method [34]. The indentation hardness is determined from the ratio of maximum load P_{max} and projected contact area

Table 2: Crystal plasticity material model parameters.

Parameter	Value
C_{11}	231.0 GPa
C_{12}	134.7 GPa
C_{44}	116.4 GPa
$\hat{\tau}_0$	50 MPa
$\hat{\tau}_{\text{sat}}$	290 MPa
p_1	26.7
p_2	5.0
h_0	961 MPa
c_1	0.025
L	1 nm
$\chi_{\alpha\beta}^{\text{GND}}$	1.0

A_c ,

$$H = \frac{P_{\max}}{A_c}. \quad (12)$$

4. Investigation of Indentation Size Effect

The indentation size effect is characterized by an increase in the apparent hardness with decreasing indentation depth [3, 4]. In particular for spherical indenters, the most important length scale corresponds to the diameter of the indenter tip. It is well known that spheres with diameters of less than 100 μm produce measurably higher hardness values [35]. Here, the ISE was investigated by combining both experimental and simulation approaches. In the first step, an indirect measurement approach for determining the hardness was described and implemented into both nanoindentation experiment and simulation. In the second step, transmission electron microscopy (TEM) was used to investigate the dislocation density in a lamella taken out of the control region underneath the indenter. In the last step, indented areas from parameterized nanoindentation simulations of two applied maximum loads (12.5 and 20 mN) were further investigated and compared with characterization results of the previous step.

A comparison between experimental and simulated hardness for different indentation loads is plotted in Figure 5(b), as absolute values, respectively.

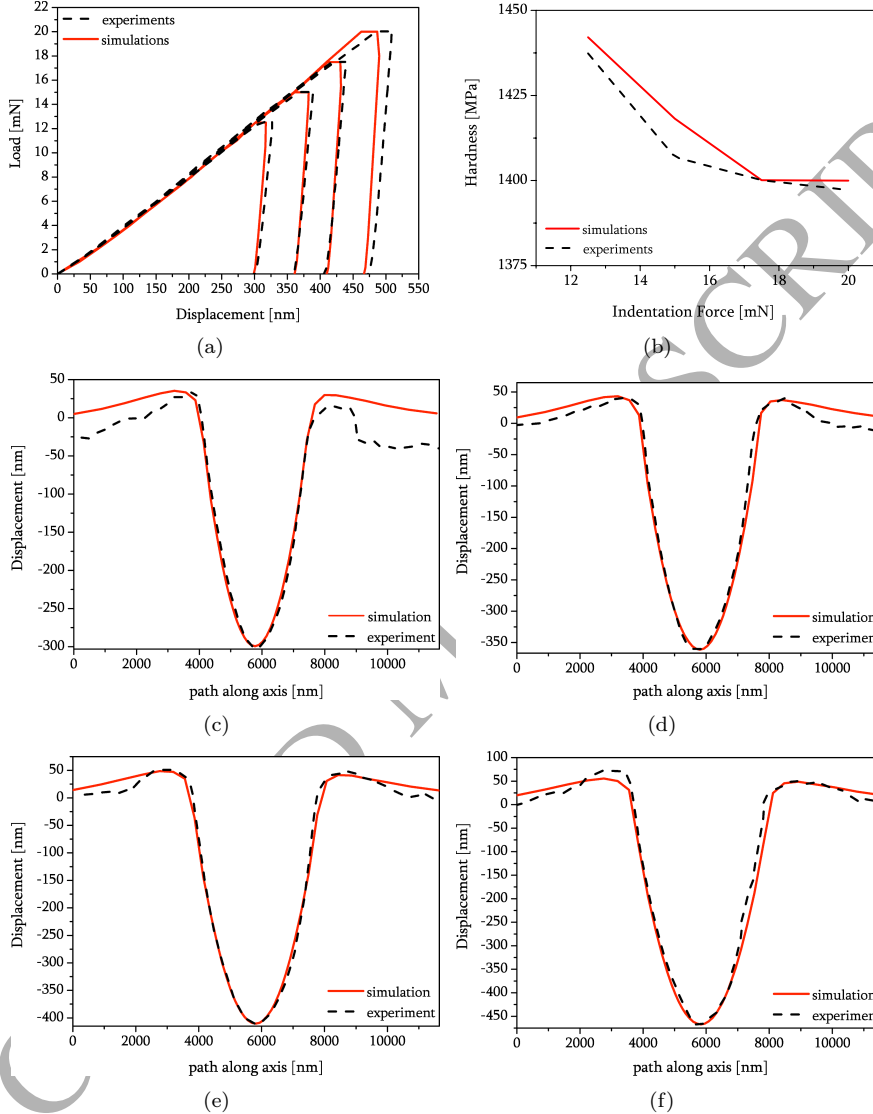


Figure 5: Overview of experimental and numerical nanoindentation results of the same grain orientation. a) represents load-displacement curves for all loading cases. Figure (b) represents the determined hardness values for both experimental and numerical nanoindentation tests. Figures(c)-(f) show the surface topology of experimental and numerical simulations with increasing indentation force (c) 12.5 mN, (d) 15 mN, (e) 17.5 mN and (f) 20 mN.

With decreasing indentation load the hardness increases, which is defined as the ISE. Furthermore, indentation hardnesses calculated from nanoindentation simulations are in a good agreement with the experiment, which proves a validity of the parameterized nanoindentation model.

4.1. Analysis of Dislocation Densities using FIB and TEM

In order to observe the dislocation substructures formed during nanoindentation a FEI Helios G4 CX focused ion beam system operated at 30 kV was used to prepare TEM specimens from indented areas of maximum applied loads of 12.5 mN and 20 mN, respectively. Low 5 kV ion beam cleaning was applied for 2 minutes to each side of TEM sample in order to remove FIB beam damage. TEM investigations were performed using FEI Tecnai Supertwin F20 equipped with high angle annular dark field (HAADF) detector operated at 200 kV. Figure 6 reveal the plastically deformed regions associated with nanoindentation. The plastically deformed volume beneath the indenter was approximated to 1.9 times the contact radius a_c and is highlighted as a dashed line in both analyzed TEM specimens in Figure 6(a) and (b). These micrographs represent multi-beam Bragg illumination contrast where the whole area below indents is clearly visible. In order to compare dislocation distributions beneath the indented regions and within the plastically deformed volume identical Bragg diffraction conditions ($g = (011)$) were used for illumination of both specimens (Fig. 6(c) and (d)). However, the dislocation densities were not directly quantified – it is clear that the microstructure shown in micrograph 6(d) after a maximum applied load of 20 mN reveals higher accumulated plastic strain than that after 12.5 mN shown in Fig. 6(c). This factor is in good agreement with former studies about the plastically deformed volume beneath a residual imprint, [36, 37]. For the case of an applied maximum load of 12.5 mN (Fig. 6(a) and (c)), dislocations homogeneously spread within this given plastically deformed volume. In contrast, TEM observation for the indent with a maximum applied load of 20 mN shows that the given plastically deformed volume covers most of the dislocations induced by the indentation test (Fig. 6(b) and (d)).

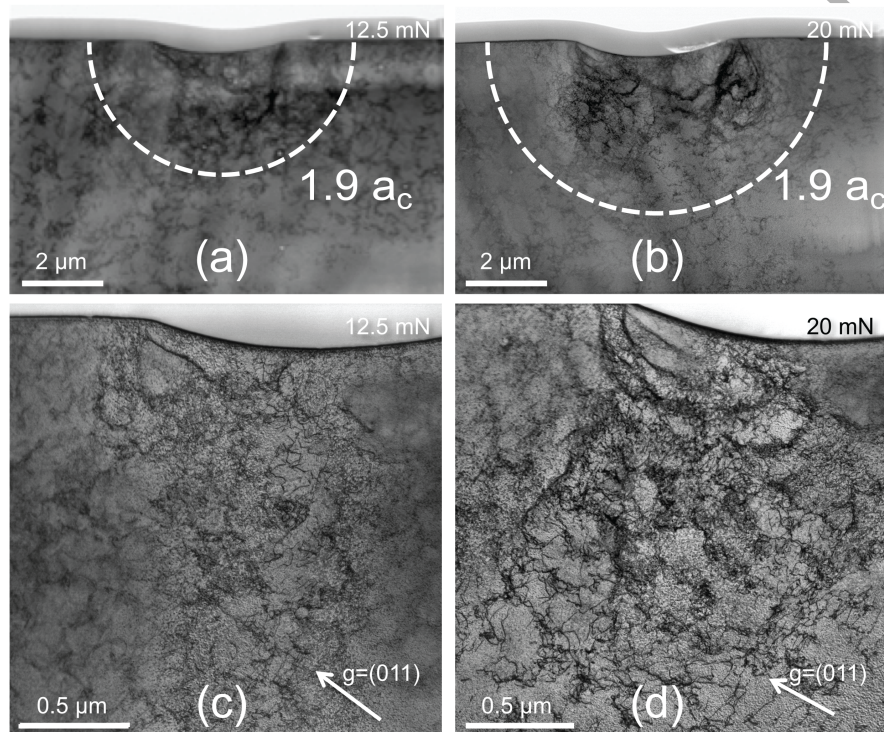


Figure 6: Dark Field Scanning Transmission Electron Microscope (TEM) image of indented sample; indentation force (a) 12.5 mN and (b) 20 mN respectively. The dashed line represents the radius of plastically deformed volume beneath the spherical indenter given as $1.9a_c$. Image (c) and (d) represents both areas of each maximum loading condition in higher magnification.

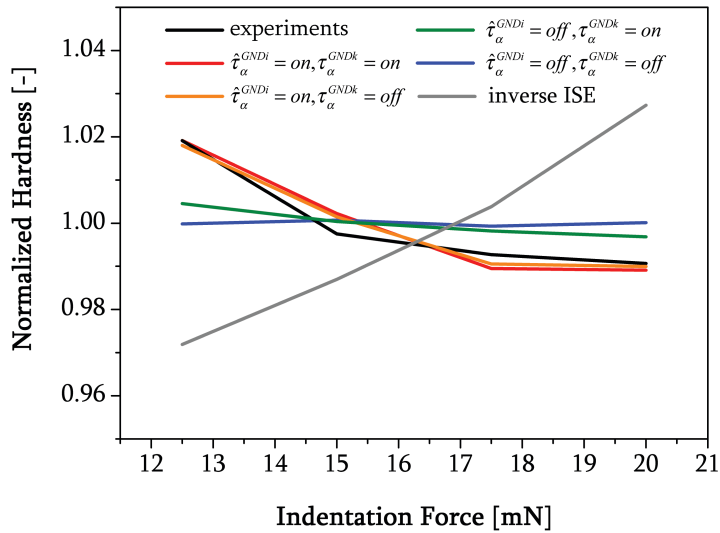


Figure 7: Plot of normalized hardness values over the maximum indentation force under consideration of different hardening models, including predicted inverse ISE by incorporating higher work hardening rates in terms of larger $\hat{\tau}_{sat}$ and h_0 values (gray).

4.2. Analysis of ISE from Nanoindentation Simulations

To investigate the role of hardening contributions on ISE, nanoindentation was simulated with three different, modified flow rule definitions: a) consideration of only $\hat{\tau}_\alpha^{GNDi}$, b) only $\hat{\tau}_\alpha^{GNDk}$ and c) excluding GND hardening terms. The result is plotted as normalized hardness values as a function of the maximum indentation force curves in Figure 7.

From this comparison it can be seen that the isotropic hardening from GNDs $\hat{\tau}_\alpha^{GNDi}$ dominates. However, ISE was not pronounced or observed for the cases of contemplating only $\hat{\tau}_\alpha^{GNDk}$ and excluding GND back stress terms. It is then worth to investigate the $\hat{\tau}_\alpha^{GNDi}$ distribution and compare with the work hardening $\hat{\tau}_\alpha$ beneath the indented region for a deeper understanding of the ISE. In addition, to study the role of higher work hardening rate on ISE, $\hat{\tau}_{sat}$ and h_0 determined in Table 2 are replaced with larger values and nanoindentation

simulations for all maximum indentation forces are performed correspondingly. As shown in Figure 7, an inverse ISE can be produced. This proves a certain flexibility of an introduced nonlocal crystal plasticity model, which allows us to predict both important observed phenomena in the nanoindentation test by balancing hardening contributions.

Therefore, the unloaded configuration for maximum indentation loads of 12.5 mN and 20 mN were evaluated. As expressed by equation (9), $\hat{\tau}_\alpha^{\text{GNDi}}$ is calculated from (super) GND densities and can be used to represent their influence while the critical resolved shear stress $\hat{\tau}_\alpha$ can be correlated to the amount of plastic deformations. Local values of $\hat{\tau}_\alpha$ and $\hat{\tau}_\alpha^{\text{GNDi}}$ evaluated from both cross-sectional and top views of the contacted region are shown in Figure 8 and 9. The plastically deformed volumes for both loading cases are determined by using the technique described above and highlighted as red-dashed lines. Within these volumes, $\hat{\tau}_\alpha$ increases continuously with maximum applied force whereas $\hat{\tau}_\alpha^{\text{GNDi}}$ remains almost constant for both maximum loading cases. According to the non-local crystal plasticity flow rule described in equation (4), the denominator or slip resistance consists of both influence of SSDs and GNDs in terms of $\hat{\tau}_\alpha$ and $\hat{\tau}_\alpha^{\text{GNDi}}$, respectively. At smaller applied forces, $\hat{\tau}_\alpha$ increases according to the work hardening and $\hat{\tau}_\alpha^{\text{GNDi}}$ is of a similar magnitude as $\hat{\tau}_\alpha$. However, for larger applied forces, $\hat{\tau}_\alpha^{\text{GNDi}}$ stagnates while $\hat{\tau}_\alpha$ continues to follow the work hardening behavior. Consequently, the hardness of the smaller applied maximum force is higher compared to the larger one. This can be understand because the radius of curvature stays constant during spherical indentation, whereas the plastic deformation and thus the work hardening constantly increases. In other words, the ISE can be captured by the introduced high-order strain gradient crystal plasticity model.

In a further step, the plastically deformed volumes beneath the indenter observed from TEM were compared with Figures 8(a) and (c), 9(a) and (c). The comparison showed how dislocations distribute in a qualitatively very similar manner below the imprint with $\hat{\tau}_\alpha^{\text{GNDi}}$ at smaller applied maximum force and similarly to $\hat{\tau}_\alpha$ at higher applied maximum force. Therefore, we concluded that

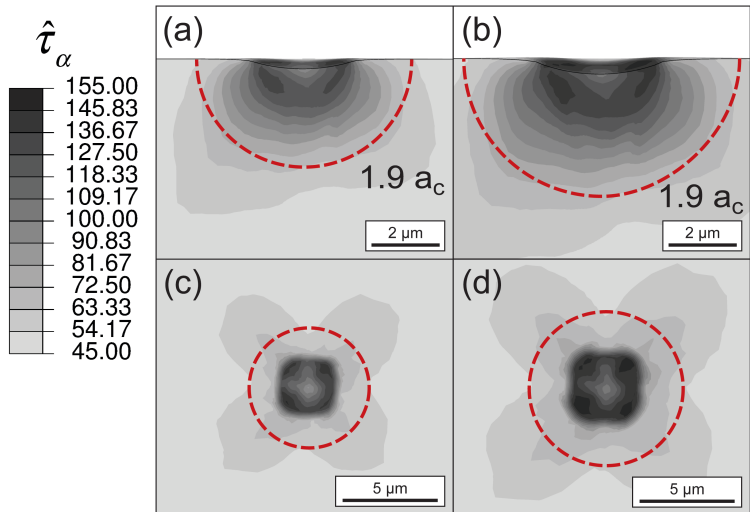


Figure 8: Contour plots of $\hat{\tau}_\alpha$ (MPa) (SSDs) under indenter tip (after unloading): (a) and (c) show SSDs for a maximum indentation force of 12.5 mN, whereas (b) and (d) show the corresponding side and top view of maximum indentation force of 20 mN. The red-dashed line represents the radius of plastically deformed volume beneath the spherical indenter.

GNDs were the dominating factor at smaller applied maximum force while SSDs were the principal contributors at the larger one.

These observations are in a good agreement with the description of ISE proposed by [4], in which different indentation tip sizes prove the concept of GNDs to start a formation of plastic impression, followed by increasingly occurring SSDs with increasing indentation forces.

5. Conclusion

In this study, concurrent experimental and numerical nanoindentation tests were performed to increase our understanding of the indentation size effect (ISE) of spherical indentations as well as the requirements for the parametrization of non-local crystal plasticity models. Nanoindentation experiments with spheri-

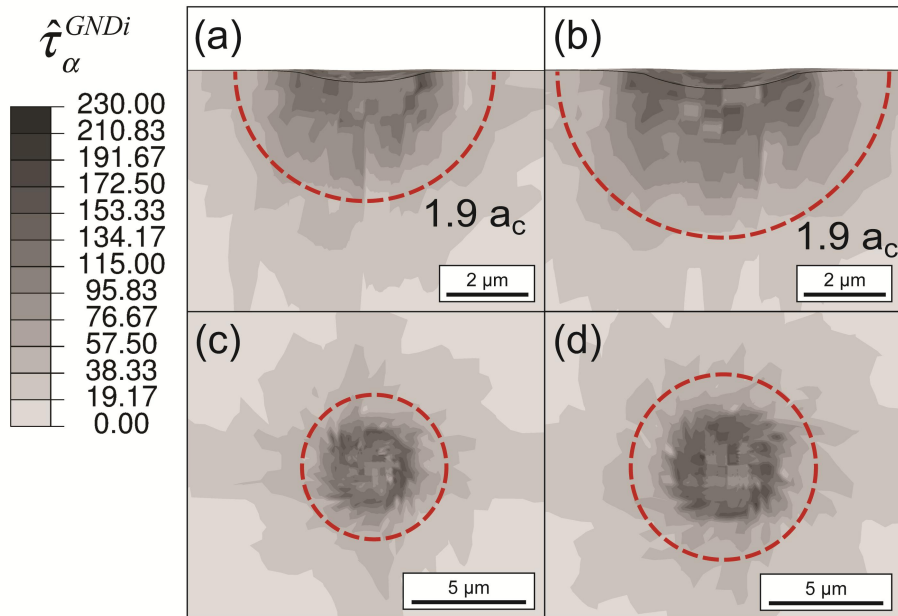


Figure 9: Contour plots of $\hat{\tau}_\alpha^{GNDi}$ (MPa) (GNDs) under indenter tip (after unloading): (a) and (c) show GNDs for a maximum indentation force of 12.5 mN, whereas (b) and (d) show the corresponding side and top view of maximum indentation force of 20 mN. The red-dashed line represents the radius of plastically deformed volume beneath the spherical indenter.

cal tips were conducted on ARMCO iron within a single grain with a crystal plane normal close to $<001>$. By using an indirect measurement method, hardness was determined, and a noticeable ISE was observed when varying applied maximum loads for the same indenter tip. An established non-local crystal plasticity model was used within Abaqus to model nanoindentation tests. With optimized material parameters, all nanoindentation simulations yielded a good agreement with obtained experimental results for load-displacement curves as well as residual imprint topology which demonstrates a robust parameterization of the model for ARMCO iron. Furthermore, comparison of experimentally and numerically obtained hardness values revealed that the indentation size effect can be reproduced with good quantitative agreement.

To understand the mechanisms of the size effect in spherical indentation, the evolution of dislocation densities was analyzed in detail, both, in experiment and numerical model. The numerical results reveal that the ratio between SSDs and GNDs with increasing indentation depth led to the observed indentation size effect. During spherical indentation, the radius of curvature of the contact area stays approximately constant, thus leading to a constant GND density. Accordingly, also the hardening contribution of GNDs is the same for small and large indentation depths. In contrast to this, the plastic strain continuously increases during spherical indentation such that the work hardening becomes more and more pronounced, which is described by an increase in SSD density in our model. It is noted here, that the material chosen for our investigation exhibits only a rather small work hardening rate. For materials with high work hardening rates, the strong increase in SSD density would overshadow the size effect because it would result in higher hardness values for larger indentation depths.

To support the observations of the numerical model, transmission electron microscopy was performed for the smallest and the largest maximum loads applied here, i.e., 12.5 and 20 mN. With increasing maximum load the amount of dislocations increased together with the plastically deformed volume, which reflects the comparatively small increase in dislocation density. The radius of the

plastic volume was approximated with $1.9a_c$, where a_c was the contact radius.

The present study demonstrates that the higher-order strain gradient plasticity model of [27] is capable of describing the ISE for spherical indents. Comparison of experiment and crystal plasticity simulations has improved our understanding of the mechanisms of the ISE by showing the different evolution of GND and SSD densities during indentation, leading to a constant hardening by GNDs and a slowly increasing work hardening by SSDs.

Acknowledgement

The authers gratefully acknowledge the scientific support of Zentrum für Grenzflächendominierte Hochleistungswerkstoffe (ZGH) of Ruhr-Universität Bochum as well as our colleagues Daysi Karina Gonzalez Dacasa and Soheil Rooein for their assistance.

References

- [1] W. C. Oliver, G. Pharr, An improved technique for determining hardness and elastic modulus using load and displacement sensing indentation experiments, *Journal of Materials Research* 7 (6) (1992) 1564–1583. doi:10.1557/JMR.1992.1564.
- [2] J. Gale, A. Achuthan, The effect of work-hardening and pile-up on nanoin-dentation measurements, *Journal of Materials Science* 49 (2014) 5066–5075. doi:10.1007/s10853-014-8213-4.
- [3] J. Swadener, E. George, G. Pharr, The correlation of the indentation size effect measured with indenters of various shapes, *Journal of the Mechanics and Physics in Solids* 50 (2002) 681–694. doi:10.1016/S0022-5096(01)00103-X.
- [4] K. Durst, M. Göken, G. Pharr, Indentation size effect in spherical and pyramidal indentations, *Journal of Physics D: Applied Physics* 41 (2008) 074005. doi:10.1088/0022-3727/41/7/074005.

- [5] D. Lucca, K. Herrmann, M. Klopfstein, Nanoindentation: Measuring methods and applications, *CIRP Annals* 59 (2010) 803–819. doi:10.1016/j.cirp.2010.05.009.
- [6] J. Nye, Some geometrical relations in dislocated crystals, *Acta Metallurgica* 1 (2) (1953) 153–162. doi:10.1016/0001-6160(53)90054-6.
- [7] E. Kröner, *Kontinuumstheorie der Versetzungen und Eigenspannungen*, Springer, Berlin, 1958.
- [8] M. F. Ashby, The deformation of plastically non-homogeneous materials, *The Philosophical Magazine: A Journal of Theoretical Experimental and Applied Physics* 21 (170) (1970) 399–424. doi:10.1080/14786437008238426.
- [9] J. Kysar, Y. Saito, M. Öztürk, D. Lee, W. Huh, Experimental lower bound on geometrically necessary dislocation density, *International Journal of Plasticity* 26 (2010) 1097–1123. doi:10.1016/j.ijplas.2010.03.009.
- [10] C. Dahlberg, Y. Saito, M. Öztürk, J. Kysar, Geometrically necessary dislocation density measurements associated with different angles of indentations, *International Journal of Plasticity* 54 (2013) 81–95. doi:10.1016/j.ijplas.2013.08.008.
- [11] N. Fleck, J. Hutchinson, A phenomenological theory for strain gradient effects in plasticity, *Journal of the Mechanics and Physics in Solids* 41 (1993) 1825–1857. doi:10.1016/0022-5096(93)90072-N.
- [12] N. Fleck, J. Hutchinson, A reformulation of strain gradient plasticity, *Journal of the Mechanics and Physics in Solids* 49 (1997) 2245–2271. doi:10.1016/0022-5096(93)90072-N.
- [13] W. Nix, H. Gao, Indentation size effects in crystalline metals: A law for strain gradient plasticity, *Journal of the Mechanics and Physics in Solids* 46 (1998) 411–425. doi:10.1016/S0022-5096(97)00086-0.

- [14] F. Roters, P. Eisenlohr, T. Bieler, D. Raabe, Crystal Plasticity Finite Element Methods, Wiley-VCH Verlag GmbH & Co KGaA, Deutschland, 2010.
- [15] R. Becker, Effects of strain localization on surface roughening during sheet forming, *Acta Materialia* 46 (4) (1998) 1385–1401. doi:10.1016/S1359-6454(97)00182-1.
- [16] M. Sachtleber, Z. Zhao, D. Raabe, Experimental investigation of plastic grain interaction, *Materials Science and Engineering: A* 336 (1) (2002) 81–87. doi:10.1016/S0921-5093(01)01974-8.
- [17] Z. Zhao, R. Radovitzky, A. Cuitiño, A study of surface roughening in fcc metals using direct numerical simulation, *Acta Materialia* 52 (20) (2004) 5791–5804. doi:10.1016/j.actamat.2004.08.037.
- [18] F. Roters, P. Eisenlohr, L. Hantcherli, D. Tjahjanto, T. Bieler, D. Raabe, Overview of constitutive laws, kinematics, homogenization and multiscale methods in crystal plasticity finite-element modeling: Theory, experiments, applications, *Acta Materialia* 58 (4) (2010) 1152–1211. doi:10.1016/j.actamat.2009.10.058.
- [19] N. Huber, C. Tsakmakis, Determination of constitutive properties from spherical indentation data using neural networks. part ii: plasticity with nonlinear isotropic and kinematic hardening, *Journal of the Mechanics and Physics of Solids* 47 (1999) 1589–1607. doi:10.1016/S0022-5096(98)00110-0.
- [20] A. Arsenlis, D. Parks, Crystallographic aspects of geometrically-necessary and statistically-stored dislocation density, *Acta Materialia* 47 (5) (1999) 1597–1611. doi:10.1016/S1359-6454(99)00020-8.
- [21] A. Arsenlis, D. M. Parks, R. Becker, V. V. Bulatov, On the evolution of crystallographic dislocation density in non-homogeneously deforming crystals, *Journal of the Mechanics and Physics of Solids* 52 (6) (2004) 1213–1246. doi:10.1016/j.jmps.2003.12.007.

- [22] L. Evers, W. Brekelmans, M. Geers, Non-local crystal plasticity model with intrinsic ssd and gnd effects, *Journal of the Mechanics and Physics of Solids* 52 (10) (2004) 2379–2401. doi:10.1016/j.jmps.2004.03.007.
- [23] M. Liu, C. Lu, K. A. Tieu, C.-T. Peng, C. Kong, A combined experimental-numerical approach for determining mechanical properties of aluminum subjects to nanoindentation, *Scientific Reports* 5 (2015) 15072 EP. doi:10.1038/srep15072.
- [24] H. Petryk, S. Stupkiewicz, S. Kucharski, On direct estimation of hardening exponent in crystal plasticity from the spherical indentation test, *International Journal of Solids and Structures* 112 (2017) 209–221. doi:10.1016/j.ijsolstr.2016.09.025.
- [25] C. Reuber, P. Eisenlohr, F. Roters, D. Raabe, Dislocation density distribution around an indent in single-crystalline nickel: Comparing nonlocal crystal plasticity finite-element predictions with experiments, *Acta Materialia* 71 (2014) 333–348. doi:10.1016/j.actamat.2014.03.012.
- [26] F. Han, B. Tang, H. Kou, J. Li, W. Wu, Y. Feng, *Nonlocal Crystal Plasticity Finite Element Simulations of Nanoindentation on Ti–6Al–4V Alloy*, Wiley-Blackwell, 2016. doi:10.1002/9781119296126.ch315.
- [27] A. Ma, A. Hartmaier, On the influence of isotropic and kinematic hardening caused by strain gradients on the deformation behaviour of polycrystals, *Philosophical Magazine* 94 (2) (2014) 125–140. doi:10.1080/14786435.2013.847290.
- [28] B. Schmaling, A. Hartmaier, Determination of plastic material properties by analysis of residual geometry of indentation, *Journal of Materials Research* 27 (2012) 2167–2177. doi:10.1557/jmr.2012.212.
- [29] C. Zambaldi, Y. Yang, T. R. Bieler, D. Raabe, Orientation informed nanoindentation of α titanium: Indentation pileup in hexagonal metals

deforming by prismatic slip, *Journal of Materials Research* 27 (2011) 356–367. doi:10.1557/jmr.2011.334.

- [30] J. Rice, Inelastic constitutive relations for solids: An internal-variable theory and its application to metal plasticity, *Journal of the Mechanics and Physics of Solids* 19 (6) (1971) 433–455. doi:10.1016/0022-5096(71)90010-X.
- [31] D. Pierce, R. Asaro, A. Needleman, An analysis of nonuniform and localized deformation in ductile single crystals, *Acta Metallurgica* 30 (1982) 1087–1119. doi:10.1016/0001-6160(82)90005-0.
- [32] S. R. Kalidindi, Incorporation of deformation twinning in crystal plasticity models, *Journal of the Mechanics and Physics of Solids* 46 (2) (1998) 267–290. doi:10.1016/S0022-5096(97)00051-3.
- [33] Dassault, Systemes, Simulia user assistance v6.14.
- [34] A. Fischer-Cripps, *Nanoindentation*, Springer-Verlag, New York, 2011.
- [35] G. Pharr, E. Herbert, Y. Gao, The indentation size effect: A critical examination of experimental observations and mechanistic interpretations, *Annual Review of Materials Research* 59 (2010) 271–292. doi:10.1146/annurev-matsci-070909-104456.
- [36] K. Durst, B. Backes, M. Göken, Indentation size effect in metallic materials: Correcting for the size of the plastic zone, *Scripta Materialia* 52 (2005) 1093–1097. doi:10.1016/j.scriptamat.2005.02.009.
- [37] J. Hua, A. Hartmaier, Determining burgers vectors and geometrically necessary dislocation densities from atomistic data, *Modelling and Simulation in Materials Science and Engineering* 18 (2010) 045007. doi:10.1088/09650393/18/4/045007.